

Fluidically innervated lattices make versatile and durable tactile sensors

Annan Zhang, Miguel Flores-Acton, Andy Yu, Anshul Gupta, Maggie Yao, Daniela Rus

Abstract— Tactile sensing plays a fundamental role in enabling robots to navigate unstructured and dynamic environments, particularly in applications such as delicate object manipulation, surface exploration, and human-robot interaction. In this paper, we introduce a passive soft robotic fingertip with integrated tactile sensing, fabricated using a 3D-printed elastomer lattice with embedded air channels. This sensorization approach, termed fluidic innervation, transforms the fingertip into a tactile sensor by detecting pressure changes within sealed air channels, providing a simple, yet robust solution to tactile sensing in robotics. Unlike conventional methods that rely on complex materials or vision-based approaches, fluidic innervation offers a simple, easily scalable, single-material fabrication process. We characterize the sensor’s response, develop a geometric model to estimate tip displacement, and train a neural network to accurately predict contact location and contact force. Additionally, we integrate the fingertip with an admittance controller to emulate spring-like behavior, demonstrate its capability for environment exploration through tactile feedback, and validate its durability under high impact and cyclic loading conditions. This tactile sensing technique offers significant advantages in terms of simplicity, adaptability, and durability, opening up new opportunities for versatile robotic manipulation.

I. INTRODUCTION

As robotic systems advance to operate in dynamic and unstructured environments, the need for tactile sensing has never been more crucial. Tactile sensors empower robots with the ability to feel and interpret physical contact, unlocking new levels of precision in tasks like object manipulation, exploration, and seamless human-robot interaction. Unlike external camera systems, which struggle with occlusions, poor lighting, or complex geometries, tactile feedback offers rich, fine-grained information about force, texture, and material properties [1], [2]. This nuanced feedback is especially important for soft robotics, where adaptability to deformation and safety are key [3], [4]. Despite the clear utility of tactile sensing, current solutions face significant challenges. These include the difficulty of integrating sensors into soft robotic structures, the fragility of many sensor designs, and the complexities of multi-material fabrication processes. Addressing these issues requires the development of more robust, scalable, and easily manufactured tactile sensors that can meet the diverse needs of real-world applications.

Tactile sensing technologies can be broadly categorized into piezoresistive, capacitive, optical, triboelectric, liquid

All authors are with the MIT Computer Science & Artificial Intelligence Laboratory (CSAIL), Massachusetts Institute of Technology, 32 Vassar St, Cambridge, MA 02139, USA.

This work was supported by the National Science Foundation EFRI grant #1830901 and the Gwangju Institute of Science and Technology.

Correspondence: zhang@csail.mit.edu

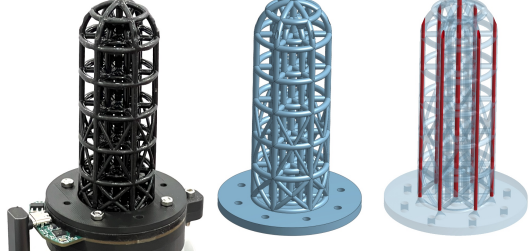


Fig. 1: Overview of our tactile robotic fingertip, featuring a 3D-printed elastomer lattice and embedded air channels for pressure-based deformation sensing. Left: Photo of the device. Middle: Render of the lattice structure. Right: Transparent render showing air channels (in red).

metal-based, and vision-based systems. Piezoresistive and capacitive sensors are widely used for their simplicity and sensitivity. Piezoresistive sensors detect pressure through changes in resistance, while capacitive sensors respond to variations in capacitance. However, both are prone to issues such as hysteresis, drift, and sensitivity to environmental noise [1], [5]. For example, piezoresistive sensors often suffer from poor repeatability and are highly sensitive to temperature, while capacitive sensors require complex signal processing to compensate for parasitic capacitance [6]. Triboelectric tactile sensors, which rely on triboelectric nanogenerators, have gained attention due to their potential for self-powered sensing. However, their limited output voltage and power supply restrict their real-time applications in continuous feedback systems [7], [8]. Vision-based tactile sensors, such as GelSight and similar systems, have gained popularity due to their high resolution and ability to capture detailed deformation information across large surfaces [9]–[21]. However, due to the high computational demands of image processing, many vision-based systems operate at low frame rates, typically between 10 and 30 Hz, which limits their use in fast, real-time tasks [14], [15], [18]. Moreover, these sensors often require elaborate lighting and optical configurations, reducing their adaptability to different environments and geometries [18], [19]. The materials used in these systems, such as gels, degrade over time, further limiting their longevity [12]. Liquid metal-based sensors provide greater flexibility, but issues related to leakage, environmental instability, and material toxicity have limited their practical applications [22]–[24]. Similarly, optoelectronic sensors offer high precision but require complex setups of waveguides and light sources, making them less suitable for use in unstructured or dynamic environments [25].

In response to these challenges, we present a novel tactile

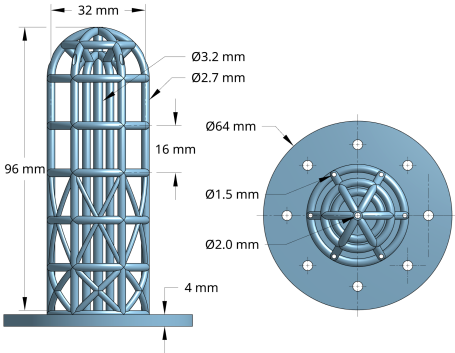


Fig. 2: Views of the rendered lattice with key measurements.

sensing approach based on fluidic innervation, which offers significant advantages in terms of simplicity, durability, and adaptability. Our method builds on prior work [26]–[28], introducing a passive soft robotic fingertip composed of a 3D-printed elastomer lattice with embedded air channels. These channels form a sealed system, allowing MEMS pressure sensors to detect deformations as pressure variations within air chambers. Unlike existing approaches that rely on complex multi-material structures or vision-based systems, fluidic innervation enables the entire tactile sensor to be fabricated using a single material in one step, simplifying the process and enhancing durability. By eliminating the need for rigid sensors or complex assembly, fluidic innervation minimizes common failure points such as stress concentrations and delamination. Moreover, 3D printing allows for rapid prototyping and customization of the fingertip's geometry, enabling us to tune its stiffness and shape for various applications without sacrificing durability. Our sensor operates at a high frequency of 200 Hz, exceeding the speed of most vision-based sensors. This makes it well-suited for fast, real-time manipulation tasks. Furthermore, our design has demonstrated exceptional durability through impact and fatigue testing, withstanding extreme deformations, impacts, and thousands of cycles without significant performance degradation. This durability is particularly notable compared to vision-based systems that rely on soft gels, which degrade under repeated use.

Through extensive mechanical characterization, we demonstrate that our fluidically innervated tactile fingertip can reliably detect forces and displacements under various loading conditions. A geometric model is developed to estimate the 3D displacement of the fingertip in response to applied forces, providing accurate insights into its behavior. Machine learning techniques are leveraged for precise contact localization and force estimation. Additionally, the fingertip is integrated into an admittance control framework, utilizing the viscoelastic properties of the lattice to mimic a linear spring with tunable stiffness, allowing the robot to interact with its environment in a controlled and nuanced manner. We further explore the sensor's potential for mapping unknown environments, showcasing its versatility in applications that rely solely on tactile feedback.

Overall, fluidic innervation offers a robust, scalable, and

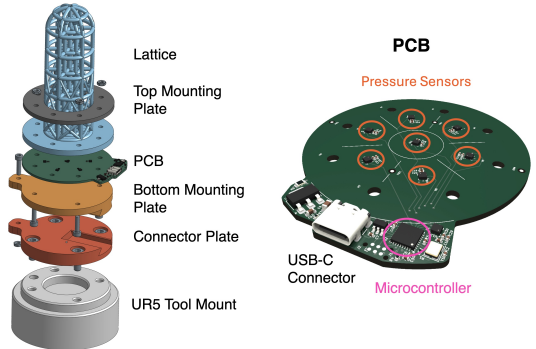


Fig. 3: Left: Assembly and close-up of the PCB.

easily fabricated approach to tactile sensing in robotics. Compared to vision-based sensors, our method provides faster response times, greater durability, and simpler fabrication, while maintaining sufficient resolution for a wide range of robotic tasks. This work opens new avenues for tactile sensing in applications requiring adaptability, real-time feedback, and long-term durability.

II. TACTILE SENSOR DESIGN

A. Lattice Design & Fabrication

As shown in Fig. 2, the lattice consists of two concentric circles (16 mm and 32 mm diameter), connected by six radial struts. Axial struts are placed at the center and where the radial and circular struts intersect, converging at the top into a dome. To prevent buckling, angled cross-struts were added in the lower sections, providing torsional stiffness near the base. These struts are thicker in the first section to ensure smooth bending under side loads. The axial, radial, and circular struts have a diameter of 2.7 mm, except for the reinforced central strut (3.2 mm). The air channels are 1.5 mm wide, with the central channel at 2 mm. The lattice has a vertical pitch of 16 mm and a total height of 96 mm. The lattice was designed in Onshape and fabricated from photosensitive elastomeric polyurethane (EPU40) using a Carbon M1 resin printer. After printing, uncured resin was removed, and the structure was cured in an oven. The lattice was then glued onto the PCB, and the air channels were sealed with epoxy.

B. Readout Electronics & Assembly

To minimize tubing and avoid interference during manipulation tasks, we positioned the sensors close to the air channels, reducing channel volume and improving temperature stability. Mounting the sensors on a custom PCB also improves manufacturability, reduces size, and lowers costs. We used LPS22HH pressure sensors, known for their wide range, temperature accuracy, and low noise. These are connected to an STM32 microcontroller via SPI, which configures the sensors and transmits pressure and temperature data at 200 Hz over USB (Fig. 3). Alternative methods for reading out fluidically innervated lattices using readily available components are discussed in previous works [26], [27]. The assembly includes 3D-printed PLA mounting plates. The lattice, PCB, and plates are screwed together and can be easily detached from the robot arm using a dovetail

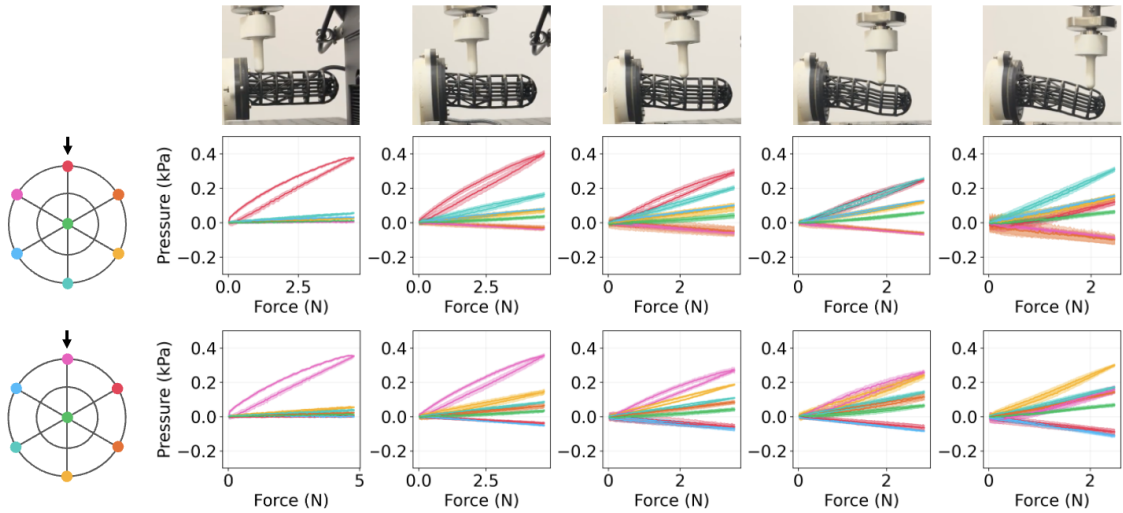


Fig. 4: Characterization of sensor responses on the mechanical testing machine. The setup shows force application at five positions along the axial direction and six orientations (two displayed here). Each plot shows the mean sensor response across five trials, with shaded regions representing ± 1 standard deviation. Responses are color-coded by sensor.

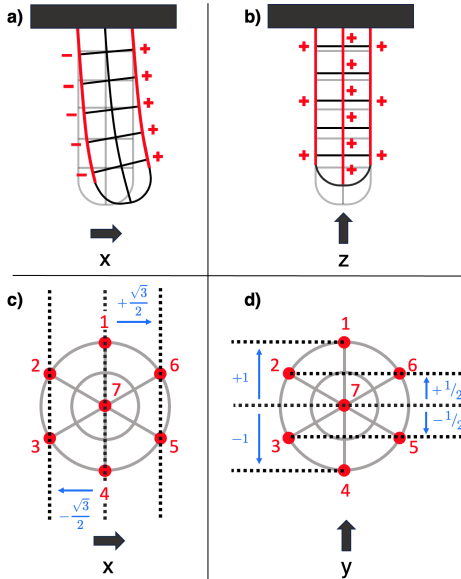


Fig. 5: Geometric modeling approach for tip displacement.

connector. The full assembly and its attachment to the UR5 robot arm are shown in Fig. 3.

III. EXPERIMENTAL EVALUATION

A. Characterization

The sensing mechanism is governed by the ideal gas law, $pV = nRT$. When confined to a closed volume, changes in pressure within the air channels can be measured as the lattice deforms. For a discussion on leakage and temperature compensation methods, refer to previous works [26], [27].

To characterize the tactile sensor's response, we applied normal forces using a universal testing machine (Instron). A 3D-printed PLA tip was used to apply compression at five discrete axial positions along the lattice, as well as six different angular orientations corresponding to the locations of the air channels' struts. The resulting sensor responses

as a function of the applied compression force are shown in Fig. 4. Each column corresponds to one of the five axial positions, with the top row showing the Instron test setup and the five positions. Each row of plots represents two of the six orientations tested. We report the mean sensor response across five trials for all seven sensors, with shaded areas denoting one standard deviation. The sensor responses are color-coded to match the air channel colors in the diagrams on the left. We make two key observations:

Position-dependent sensor response: When force is applied near the base (first column), the top channel shows a strong response, while other channels remain mostly unresponsive. Conversely, when force is applied near the tip (last column), the strongest response comes from the diametrically opposite channel (i.e., the bottom), as the lattice bends downward. The top channel experiences a superposition of direct compression (positive pressure) and tension from bending (negative pressure), causing a weaker net response. For intermediate positions, we observe a gradual transition between these extremes, with the top channel's response weakening and the bottom channel's response strengthening as force moves from the base to the tip. This behavior is consistent with previous observations in fluidically innervated grippers, where a superposition of direct compression and bending deformations was identified [27].

Orientation-dependent symmetry: Due to the 60-degree rotational symmetry of the lattice and air channel structure, we expect qualitatively similar sensor responses for different orientations, with only the specific channels activated varying. This is confirmed by the similarity in sensor responses between the first and second rows, where the lattice was rotated by 60 degrees clockwise.

B. 3D Tip Displacement Estimation

For external forces acting at the fingertip, we develop a geometric approach to estimate the 3D displacement of the

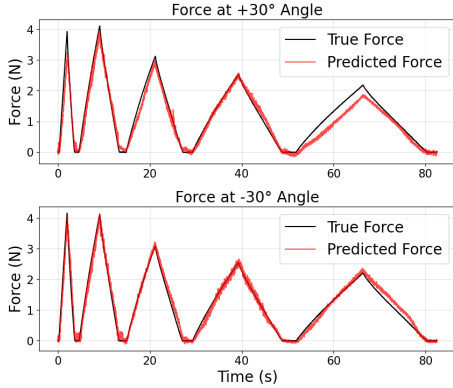


Fig. 6: Predicted force vs. ground truth for 5 positions at 30° and -30° , showing strong prediction accuracy for both positions.

fingertip. An external force applied in the positive x -direction induces bending that moves the tip in the positive x -direction, leading to positive pressure readings on the compression side and negative readings on the tension side (see Fig. 5a). This behavior aligns with observations in previous work [26]. We evaluate each pressure channel: the more its pressure value matches the expected pattern under a positive x -force (e.g., positive pressures for channels 5 and 6, negative pressures for channels 2 and 3 as shown in Fig. 5c), the more confident we are of a force in the positive x -direction. The magnitude of the force correlates with the magnitude of the measured pressure change [27]. The extent to which each channel is compressed or stretched depends on its normal distance from the neutral plane (depicted as the vertical dotted line in the center of Fig. 5c). Therefore, we weight each sensor reading by its normal distance from the neutral plane in the cross-section. A similar argument applies for the y -direction, but the weights differ due to the 60-degree separation of the channels (see Fig. 5d). When the tip moves in the z -direction, the direct compression of the center strut results in a positive reading in the channel 7 (see Fig. 5b). To ensure that effects on the displacement estimate cancel out if all channel pressures increase by the same constant amount (e.g., due to ambient temperature changes in a closed volume), the weights are designed to sum to zero. This approach leads to the following equations for estimating the tip displacements:

$$\delta_x = \alpha_x \left(\frac{\sqrt{3}}{2} (p_5 + p_6 - p_2 - p_3) \right) \quad (1)$$

$$\delta_y = \alpha_y \left(p_1 - p_4 + \frac{1}{2} (p_2 - p_3 - p_5 + p_6) \right) \quad (2)$$

$$\delta_z = \alpha_z \left(p_7 - \frac{1}{6} (p_1 + p_2 + p_3 + p_4 + p_5 + p_6) \right) \quad (3)$$

where δ_i are the estimated displacements from the pressure readings, α_i are scaling parameters to be identified, and p_1, p_2, \dots, p_7 are the deformation-induced pressure changes.

C. Contact Location & Force Detection

Detecting forces acting along the cylindrical part of the device is more complex than detecting those at the tip.

Deformations in this region compress individual channels, leading to highly non-linear and time-dependent effects. As shown in Section III-A, even applying normal forces with the Instron results in distinct sensor signals. The material's large deformations and non-linear constitutive behavior further complicate modeling. However, based on the characterization data, we observe a clear qualitative difference between contacts at the top and bottom, making it feasible to estimate the axial force location. The radial force location can be deduced from which channels are activated, as they are positioned differently around the circumference. Furthermore, higher forces generally produce stronger sensor signals, allowing us to estimate force magnitude.

To achieve accurate contact location and force predictions, we use a machine learning-based approach. A neural network (NN) is trained on data from our characterization experiments, where forces were applied at 5 axial positions and 6 radial angles, repeated over 5 trials. The NN takes in the 7 sensor values at each timestep and simultaneously predicts the contact location (as one of 6 radial angles and one of 5 axial positions) and the force magnitude. Following the approach in [29], we collected an additional trial as a test set to validate the model. We used a fully connected neural network with 2 hidden layers, each containing 128 neurons. The model, containing 37K parameters, trained in under 3 minutes on a desktop PC with an RTX 3090 GPU. On the test set, the NN achieved a classification accuracy of 95% for the axial position, 99% for the radial angle, and a mean absolute error (MAE) of 0.16 N for force predictions. Fig. 6 shows predicted force vs. ground truth for 5 positions at two angles: one at 30° (with a force MAE of 0.17 N), and one at -30° (with a force MAE of 0.12 N). The NN's forward pass is extremely fast (0.29 ± 0.04 ms), making it suitable for real-time applications. This processing speed allows us to fully utilize the 200 Hz data rate of our sensor, a common issue with many vision-based solutions.

While our setup demonstrates promising results, additional work is required to adapt this approach for real-world manipulation tasks, where contact patches are more complex (e.g., larger areas instead of point contacts), and forces act in arbitrary directions. This experiment shows that even with a simple NN and no historical data, we can extract rich and accurate information about contact location and applied force from only 7 sensor channels.

D. Admittance Control with Tunable Stiffness

To demonstrate the fingertip's capabilities, we implemented an admittance control scheme that enables the robot arm's end-effector to behave like a linear spring. In this setup, the force required to displace the tip increases linearly with the displacement, and the spring stiffness can be individually tuned along each axis (k_x, k_y, k_z). Since our robot (UR5) is position-controlled, we respond to external forces applied at the fingertip by reading the pressure signals, estimating the tip displacements using the geometric approach from Section III-B, and computing position commands for the

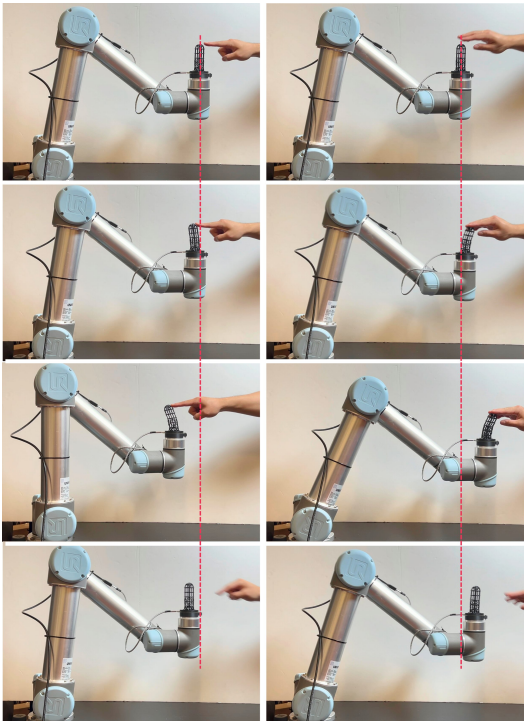


Fig. 7: Sequence of images from a video demonstrating the spring-like behavior of the robot tip running the admittance controller. As a horizontal force is applied and then removed, the robot moves back towards its original position (marked by dashed red line).

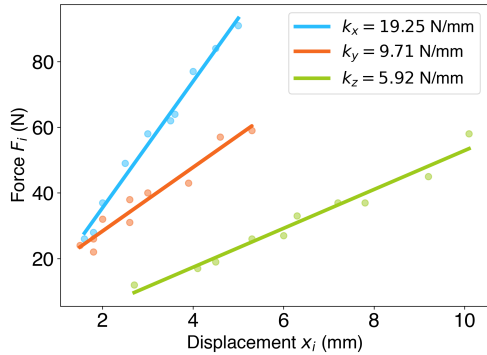


Fig. 8: Effective stiffness measurements in each direction for the admittance controller, with linear least squares fit.

UR5. The control law is defined as:

$$u_i = \beta_i \delta_i, \quad \text{for } i \in \{x, y, z\} \quad (4)$$

where u_i is the commanded position of the UR5 end-effector in the i -th direction, δ_i is the estimated tip displacement from Eqns. (1)–(3), and β_i is the control gain for the i -th direction. To achieve a natural interaction feel, we select:

$$\alpha_x \beta_x = \alpha_y \beta_y = \frac{1}{15}, \quad \alpha_z \beta_z = \frac{1}{7.5} \quad (5)$$

With these gains, the robot responds to fingertip displacements in a way that simulates a virtual spring, providing tactile feedback to the user. We experimentally determined the effective stiffnesses k_x , k_y , and k_z corresponding to these gain settings. For each direction, we applied 10 different

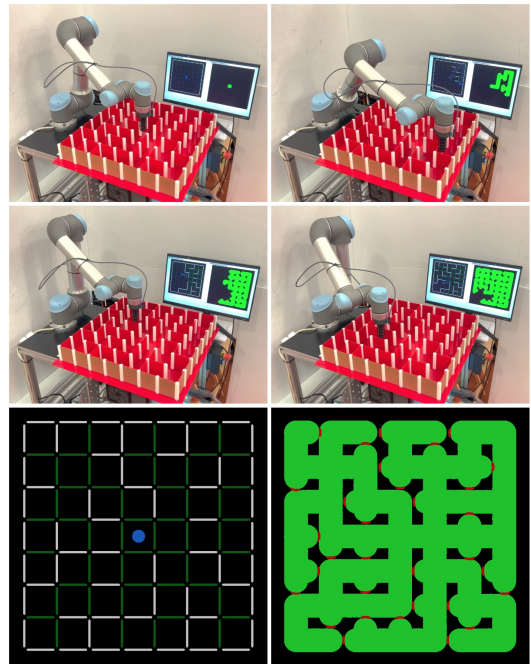


Fig. 9: Tactile exploration of a maze. Top: Robot stages while exploring and the evolving knowledge of the maze displayed on a monitor. Bottom: Final exploration result, showing lattice traversed regions (green) and contact points (red) on the right, and inferred walls (white) and open spaces (green) on the left.

forces F_i to the tip using a handheld force gauge and recorded the corresponding total displacements $x_i = \delta_i + u_i$. We then plotted the force versus displacement data and performed a linear least squares fit to determine the effective stiffness as $k_i = \frac{F_i}{x_i}$. The stiffness measurements are displayed in Fig. 8, along with the linear fits. Fig. 7 illustrates the spring-like behavior of the robot tip under the admittance controller. When the user applies a horizontal force, the robot moves back, and upon releasing the force, the robot returns to its original position. We show clips of different interactions in the supplementary video.

E. Tactile Exploration & Mapping

We demonstrate our tactile sensor's ability to explore and map unknown environments in a 2D maze task. To detect obstructions and open spaces, the environment is divided into $1 \text{ mm} \times 1 \text{ mm}$ cells for an effective balance between resolution and efficiency. Fig. 9 bottom row shows a heuristic cell map (right) and a simplified maze abstraction (left). This approach can extend to more complex or 3D environments, but here we focus on demonstrating effective tactile exploration with our fingertip, using the geometric model from Section III-B. The contact surface is determined by the lattice radius, tip displacement, and thickness parameters, with δ_x and δ_y (from Eqns. (1)–(2)) estimating contact location. The contact angle is computed using $\arctan_2(\delta_x, \delta_y)$, and an arc with radius and span defines the contact surface.

For maze exploration, the robot moves in a constrained x-y direction, advancing as long as the tip displacement

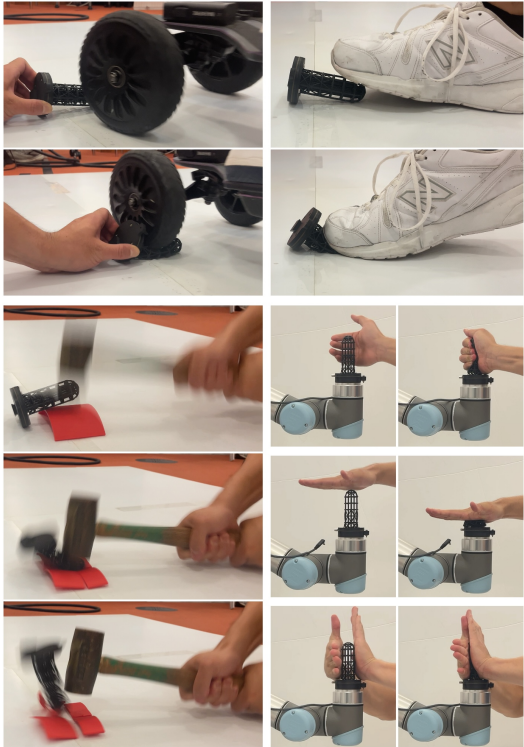


Fig. 10: The lattice subjected to high-impact loading and extreme deformations, including squeezing and stepping, as well as being hammered and run over by an electric skateboard.

stays below a threshold. If the sensor detects an obstruction, the robot marks the edge as a wall and returns to the previous cell. Otherwise, the edge is marked clear, and the new cell is added to the depth stack. The maze is explored using a Depth First Search (DFS) algorithm, with the robot checking neighboring cells based on three criteria: the cell is within the maze, not in the depth stack, and connected by an undefined wall. Boundary edges are treated as walls. The robot recursively explores unexplored cells, backtracking when no valid options remain. The experiment was repeated with various maze configurations, consistently identifying all walls correctly, as shown in the supplementary video.

F. Durability against Impact and Fatigue

We demonstrate the durability of the lattice and the entire device by subjecting it to extreme impact and deformation tests. Shown in Fig. 10, the lattice is compressed top-down, side-to-side, and radially while mounted. Additionally, the device was subjected to extreme loading, with an 80 kg individual stepping on it and a person riding over it on an electric skateboard (weight 70 kg). To test resistance to high peak forces, we struck the device with a hammer, generating enough impact to crack a 3 mm thick PLA sheet beneath it. Uncut video clips in the supplementary material show the full sequence, where we run the admittance control demo from section III-D, unplug and dismount the device, subject it to these extreme tests, and then remount it on the robot arm, demonstrating that it still functions. During the filming

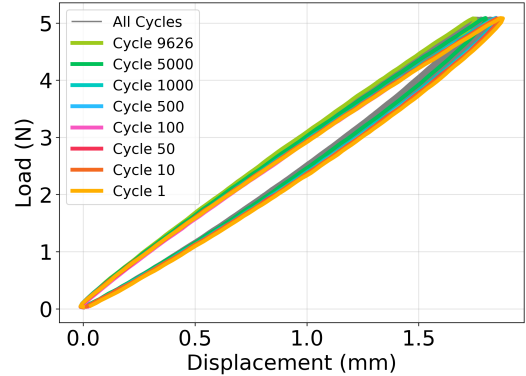


Fig. 11: Force-displacement cycles during fatigue testing.

process, we subjected the same device to numerous hammer blows, stepping tests, and skateboard rolls before and after the final recordings. After further deliberate stress tests, including hammer blows and dropping an 8 lb weight, parts of the PCB chipped off and the mounting plate detached, rendering the device unmountable on the robot arm. Despite this, the tactile sensing remained functional, and the device could still be used as a joystick to control the UR5 tip. The device ultimately failed when additional hammer blows interrupted the PCB's electrical traces.

To evaluate the device's durability under fatigue, we subjected it to cyclic loading using an Instron machine. The Instron was set to 1 mm/s for 10,000 cycles, applying forces from 0.05 to 5.05 Newtons to maintain contact (with the setup as in Fig. 4 top left plot). The displacement gauge was reset before each loading cycle. The first five cycles were discarded due to stress softening of the elastomeric polyurethane. After filtering out cycles with NaN values, 9,626 cycles were retained for analysis. The resulting force-displacement plot over all cycles is shown in Fig. 11. All cycles are plotted in grey, with the 1st, 50th, 100th, 500th, 1,000th, 5,000th, and final 9,626th cycles highlighted in color. Remarkably, the cycles overlap almost entirely, even after nearly 10,000 repetitions, suggesting that the lattice is highly durable against fatigue. However, further work is needed to assess how the mechanical properties and sensor responses evolve over prolonged cycling, and how many cycles the device can ultimately withstand.

IV. CONCLUSION

The introduction of fluidic innervation in a passive soft robotic fingertip provides a simple yet effective solution to tactile sensing, offering enhanced adaptability and durability. This approach leverages a scalable, single-material fabrication process that detects pressure changes within air channels, eliminating the complexity of conventional methods. By integrating the fingertip with an admittance controller and validating its performance under various conditions, we demonstrate its potential for a wide range of robotic applications, from delicate manipulation to environmental exploration. This work opens up new opportunities for more robust and versatile robotic manipulation in unstructured and dynamic environments.

REFERENCES

- [1] H. Yousef, M. Boukallel, and K. Althoefer, “Tactile sensing for dexterous in-hand manipulation in robotics—a review,” *Sensors and Actuators A: physical*, vol. 167, no. 2, pp. 171–187, 2011.
- [2] R. S. Dahiya, G. Metta, M. Valle, and G. Sandini, “Tactile sensing—from humans to humanoids,” *IEEE transactions on robotics*, vol. 26, no. 1, pp. 1–20, 2009.
- [3] D. Rus and M. T. Tolley, “Design, fabrication and control of soft robots,” *Nature*, vol. 521, no. 7553, pp. 467–475, 2015.
- [4] S. Kim, C. Laschi, and B. Trimmer, “Soft robotics: a bioinspired evolution in robotics,” *Trends in biotechnology*, vol. 31, no. 5, pp. 287–294, 2013.
- [5] Y. Peng, N. Yang, Q. Xu, Y. Dai, and Z. Wang, “Recent advances in flexible tactile sensors for intelligent systems,” *Sensors*, vol. 21, no. 16, p. 5392, 2021.
- [6] X. Ji, X. Zhao, M. C. Tan, and R. Zhao, “Artificial perception built on memristive system: Visual, auditory, and tactile sensations,” *Advanced Intelligent Systems*, vol. 2, no. 3, p. 1900118, 2020.
- [7] D. Choi, Y. Lee, Z.-H. Lin, S. Cho, M. Kim, C. K. Ao, S. Soh, C. Sohn, C. K. Jeong, J. Lee, et al., “Recent advances in triboelectric nanogenerators: from technological progress to commercial applications,” *ACS nano*, vol. 17, no. 12, pp. 11087–11219, 2023.
- [8] Y. Lin, S. Duan, D. Zhu, Y. Li, B. Wang, and J. Wu, “Self-powered and interface-independent tactile sensors based on bilayer single-electrode triboelectric nanogenerators for robotic electronic skin,” *Advanced Intelligent Systems*, vol. 5, no. 4, p. 2100120, 2023.
- [9] W. Yuan, S. Dong, and E. H. Adelson, “Gelsight: High-resolution robot tactile sensors for estimating geometry and force,” *Sensors*, vol. 17, no. 12, p. 2762, 2017.
- [10] O. Azulay, N. Curtis, R. Sokolovsky, G. Levitski, D. Slomovik, G. Lilling, and A. Sintov, “Allsight: A low-cost and high-resolution round tactile sensor with zero-shot learning capability,” *IEEE Robotics and Automation Letters*, vol. 9, no. 1, pp. 483–490, 2023.
- [11] S. Quan, X. Liang, H. Zhu, M. Hirano, and Y. Yamakawa, “Hivtac: A high-speed vision-based tactile sensor for precise and real-time force reconstruction with fewer markers,” *Sensors*, vol. 22, no. 11, p. 4196, 2022.
- [12] W. K. Do and M. Kennedy, “Densetact: Optical tactile sensor for dense shape reconstruction,” in *2022 International Conference on Robotics and Automation (ICRA)*. IEEE, 2022, pp. 6188–6194.
- [13] W. K. Do, B. Jurewicz, and M. Kennedy, “Densetact 2.0: Optical tactile sensor for shape and force reconstruction,” in *2023 IEEE International Conference on Robotics and Automation (ICRA)*. IEEE, 2023, pp. 12549–12555.
- [14] H. Sun, K. J. Kuchenbecker, and G. Martius, “A soft thumb-sized vision-based sensor with accurate all-round force perception,” *Nature Machine Intelligence*, vol. 4, no. 2, pp. 135–145, 2022.
- [15] B. Ward-Cherrier, N. Pestell, L. Cramphorn, B. Winstone, M. E. Giannaccini, J. Rossiter, and N. F. Lepora, “The tactip family: Soft optical tactile sensors with 3d-printed biomimetic morphologies,” *Soft robotics*, vol. 5, no. 2, pp. 216–227, 2018.
- [16] A. Zhang, R. L. Truby, L. Chin, S. Li, and D. Rus, “Vision-based sensing for electrically-driven soft actuators,” *IEEE Robotics and Automation Letters*, vol. 7, no. 4, pp. 11509–11516, 2022.
- [17] T. Zhang, Y. Cong, X. Li, and Y. Peng, “Robot tactile sensing: Vision based tactile sensor for force perception,” in *2018 IEEE 8th Annual International Conference on CYBER Technology in Automation, Control, and Intelligent Systems (CYBER)*. IEEE, 2018, pp. 1360–1365.
- [18] E. Roberge, G. Fornes, and J.-P. Roberge, “Stereotac: A novel visuo-tactile sensor that combines tactile sensing with 3d vision,” *IEEE Robotics and Automation Letters*, 2023.
- [19] M. H. Tippur and E. H. Adelson, “Gelsight360: An omnidirectional camera-based tactile sensor for dexterous robotic manipulation,” in *2023 IEEE International Conference on Soft Robotics (RoboSoft)*. IEEE, 2023, pp. 1–8.
- [20] D. F. Gomes, Z. Lin, and S. Luo, “Geltip: A finger-shaped optical tactile sensor for robotic manipulation,” in *2020 IEEE/RSJ International Conference on Intelligent Robots and Systems (IROS)*. IEEE, 2020, pp. 9903–9909.
- [21] A. Padmanabha, F. Ebert, S. Tian, R. Calandra, C. Finn, and S. Levine, “Omnitact: A multi-directional high-resolution touch sensor,” in *2020 IEEE International Conference on Robotics and Automation (ICRA)*. IEEE, 2020, pp. 618–624.
- [22] Y. Wang, J. Jin, Y. Lu, and D. Mei, “3d printing of liquid metal based tactile sensor for simultaneously sensing of temperature and forces,” *International Journal of Smart and Nano Materials*, vol. 12, no. 3, pp. 269–285, 2021.
- [23] Y. Ren, X. Sun, and J. Liu, “Advances in liquid metal-enabled flexible and wearable sensors,” *Micromachines*, vol. 11, no. 2, p. 200, 2020.
- [24] J. Qin, D. Cui, L. Ren, W. Hao, Y. Shi, and Y. Du, “Emerging advances of liquid metal toward flexible sensors,” *Advanced Materials Technologies*, vol. 9, no. 14, p. 2300431, 2024.
- [25] H. Zhao, K. O’Brien, S. Li, and R. F. Shepherd, “Optoelectronically innervated soft prosthetic hand via stretchable optical waveguides,” *Science robotics*, vol. 1, no. 1, p. eaai7529, 2016.
- [26] R. L. Truby, L. Chin, A. Zhang, and D. Rus, “Fluidic innervation sensorizes structures from a single build material,” *Science Advances*, vol. 8, no. 32, p. eabq4385, 2022.
- [27] A. Zhang, L. Chin, D. L. Tong, and D. Rus, “Embedded air channels transform soft lattices into sensorized grippers,” in *2024 IEEE International Conference on Robotics and Automation (ICRA)*. IEEE, 2024, pp. 5264–5270.
- [28] V. K. Chen, L. Chin, J. Choi, A. Zhang, and D. Rus, “Real-time grocery packing by integrating vision, tactile sensing, and soft fingers,” in *2024 IEEE 7th International Conference on Soft Robotics (RoboSoft)*. IEEE, 2024, pp. 392–399.
- [29] A. Zhang, T.-H. Wang, R. L. Truby, L. Chin, and D. Rus, “Machine learning best practices for soft robot proprioception,” in *2023 IEEE/RSJ International Conference on Intelligent Robots and Systems (IROS)*. IEEE, 2023, pp. 2564–2571.